이학석사 학위논문

과산소-유도 ΔR1: 뇌졸중에서 뇌 손상의 자기공명영상 바이오마커

Hyperoxia-induced ΔR1: MRI biomarker of cerebral damage in stroke

울산대학교 대학원

의 학 과

신 기 창

과산소-유도 ΔR1: 뇌졸중에서 뇌 손상의 자기공명영상 바이오마커

지도교수 김 정 곤

이 논문을 이학석사 학위 논문으로 제출함

2017년 12월

울산대학교 대학원

의 학 과

신 기 창

신기창의 이학석사학위 논문을 인준함

심사위원 김 정 곤 (인)

심사위원 신 희 정 (인)

심사위원 심 우 현 (인)

울 산 대 학 교 대 학 원

2017 년 12 월

Abstract (English)

Non-invasive imaging of tissue oxygenation provides important information about stroke-induced cerebral damage. Here, we introduce a MRI parameter, hyperoxia-induced ΔR_1, which quantifies oxygen-derived R_1 change during hyperoxic respiration. In transient stroke rats, the ischemic brain demonstrated a significant elevation of hyperoxia-induced ΔR_1 depending on the ischemic severity (defined by apparent diffusion coefficient), which indicated stroke-driven excessive oxygen accumulation. One possible cause of the ΔR_1 increase was uncontrolled plasma-to-tissue oxygen flux due to neurovascular disruption, presented by a significant correlation between ΔR_1 and vasogenic edema (R_2 value) and by a different hyperoxia-driven ΔPtO_2 pattern (fiberoptic oxymetry) between ischemic (non-plateaued increase) and non-ischemic brain (rapid arrival at plateau). Reduced oxygen consumption was also suggested to increase ΔR_1 according to a significant inverse correlation between ΔR_1 and glucose metabolism activity (^{18}F-FDG uptake). The image parameters of ischemic damage including apparent diffusion coefficient, vasogenic edema (R_2), capillary volume (ΔR_2 driven by superparamagnetic iron oxide agent) and glucose metabolism (^{18}F-FDG uptake) showed a dichotomized distribution according to the ΔR_1. Therefore, the hyperoxia-induced ΔR_1 can classify the status of ischemic brain as "exacerbating" and "devastated" stage. Conclusively, the hyperoxia-induced ΔR_1 can be a relevant MRI biomarker to assess stroke-induced cerebral damage.

Keywords: tissue oxygenation, R1, Non-invasive imaging, MRI biomarker, stroke, Hyperoxia-induced ΔR1

Table of contents

List of tables, figures

Introduction

Cerebral oxygenation, a critical index of brain function and vitality, is closely and reciprocally related to neurovascular oxygen supply and cellular oxygen consumption. Quantitative assessment of cerebral oxygenation status can therefore provide relevant information on stroke-induced damage in the cerebral vasculature and neurons [1-3]. From a clinical perspective, a biomarker reflecting impaired oxygen delivery/demand would be valuable for treatment planning and prognosis prediction in the management of stroke patients.

To spatially demonstrate the cerebral oxygenation status, a number of non-invasive diagnostic tools have been investigated. Blood oxygen level-dependent magnetic resonance imaging (MRI) has been intensively studied as a high-resolution imaging tool to indirectly measure the tissue oxygenation level from deoxyhemoglobin (deoxyHb)-derived T_2^* contrast [4-6]. Although widely applied, this method is challenged by the magnetic field vulnerability to various factors other than deoxyHb as well as by the complexity in calculating tissue oxygenation (PtO_2) from the MRI signal [4]. As a molecular imaging method, positron emission tomography (PET) using various radiotracers, such as ^{18}F-FAZA, ^{18}F-FETNIM and ^{64}Cu-ATSM, can visualize the level of tissue hypoxia. However, the requirement for tracer-producing facilities and complex tracer kinetic modelling has limited the widespread application of PET-based approaches [7, 8].

As an alternative to overcome the limitation of existing methods, investigators have explored the oxygen-induced *in vivo* T_1 contrast effect on MRI, which can be readily generated by oxygen breathing [4, 9-13]. Theoretically, oxygen-driven acceleration of longitudinal relaxation (quantified by increased R_1) during hyperoxic challenge can directly indicate the amount of tissue oxygen accumulation, which also reflects the baseline oxygenation [14]. Based on this physical background, hyperoxia-induced ΔR_1 has demonstrated the eligibility to quantify the tumor hypoxia in the name of 'tissue-oxygenation-level dependent MRI' or 'oxygen-enhanced MRI' [14-16]. However, this imaging biomarker has not been used to evaluate the hypoxic-ischemic cerebral injury despite the tissue oxygenation is of critical importance for the restoration of cerebral structure and function.

In order to utilize the hyperoxia-induced ΔR_1 in stroke evaluation, organ- and disease-oriented validation is mandatory due to the uniqueness of cerebral vascular and cellular environment. As the cerebral oxygen level is determined by the balance between oxygen delivery and consumption, neurovascular integrity and neuronal glucose metabolism are important for the interpretation of hyperoxia-induced oxygen accumulation in stroke brain. In this context, it is worth analysing the relationship of hyperoxia-induced ΔR_1 with vasogenic edema severity, blood volume and ^{18}F-fluorodeoxyglucose (FDG) uptake. In particular, such approach may help to determine the ability of this imaging

biomarker to classify the potential of cerebral tissue to restore from ischemic damage.

Here, we investigated whether hyperoxia-induced ΔR_1 adequately indicates the cerebral oxygenation in transient stroke rats, using PtO_2 measured by fibreoptic tissue oximetry as a reference. Thereafter, voxel-wise correlation of the ΔR_1 with image parameters indicating cellular/vasogenic edema, vascular parameters and glucose metabolism was analysed on co-registered MR and/or PET images. Based on these experiments, we finally discuss the potential use of hyperoxia-induced ΔR_1 as a biomarker to evaluate the cerebral damage in stroke.

Materials and Methods

Animal care and experimental procedures in this study were approved by the Institutional Animal Care and Use Committee of the Korea Basic Science Institute (KBSI-AEC 1413).

Transient stroke model

A total of 19 adult male Wistar rats (13 transient stroke rats and 6 control rats) weighing 280 to 300 g were used. Transient stroke was induced by temporally occluding the right middle cerebral artery (MCA)for 60 min. The rats were anaesthetized with 1.5% isoflurane in 70% N_2O/30% O_2 (flow rate, 1.0 l/min), and then MCA was occluded using

the intraluminal filament technique as previously described [17]. In brief, the common carotid artery and the proximal pterygopalatine artery were ligated using 4-0 silk suture. Thereafter, the superior thyroid and occipital branches of the external carotid artery were transected. Finally, a silicon rubber-coated 5-0 nylon monofilament (tip diameter, 0.31 ± 0.02 mm) was advanced 17 to 18 mm to the bifurcation along the internal carotid artery to occlude the MCA. After 60 min of MCA occlusion, the filament was carefully withdrawn to induce vascular re-canalization. All experiments in this study were performed approximately 24 h after transient MCA occlusion.

Gas paradigm

PtO_2, PaO_2, SaO_2, and MRI parameters were measured in each of normoxic (20% oxygen) and hyperoxic respiration (100% oxygen). Normoxic and hyperoxic gases were infused through a respiratory mask without mechanical ventilation. The gas flow rate (1 l/min at 1 atmosphere) was constant during the experiment while the inhaled gas mixture was manually switched using a multichannel flowmeter.

PtO_2, PaO_2 and SaO_2 measurement

To assess the evidence supporting the oxygen-derived generation of ΔR_1 during hyperoxic challenge, the tissue and blood oxygen concentration was measured in both

normoxic and hyperoxic respiration. The PtO_2 was measured during baseline normoxia (FiO_2, 20%; 5 min), hyperoxia (FiO_2, 100%, 5 min) and second normoxia (FiO_2, 20%; 10 min) in both ischemic and non-ischemic brain using a fibreoptic oximetry unit (Oxylite, Oxford Optronics, UK). To measure PtO_2 in the ischemic brain, the stroke area was identified by diffusion-weighted imaging and ADC mapping. In each rat, two implantable fibre optic leads with a fluorescent tip were inserted in the ipsilateral and contralateral hemispheres while the animal's head was fixed in a stereotaxic head holder. The holes were generated 1-mm superior and 4-mm lateral to the bregma, leaving the dura intact, and the tip of the fibre optic lead was advanced 4 mm below the dura. To avoid the initial fluctuation, the PtO_2 was measured approximately 10 min after the probe insertion. The signals were continuously monitored at a rate of 200 Hz.

Blood gas analyses were performed to measure the partial pressure of oxygen (PaO_2) and oxygen saturation rate (SaO_2) at normoxia and hyperoxia in the arterial blood using a blood gas analyzer (i-STAT, Abbott Laboratories Inc, USA) as described previously [13].

MRI

All MRI experiments were performed using a 4.7-T unit (BioSpec, Bruker, Enlangen, Germany) that was equipped with a 72-mm transmit-only volume coil and a

receive-only surface coil. Rats were positioned on a custom-made cradle and anaesthetized with 1.5% to 2.0% isoflurane inhalation through a mask. A body temperature of 37 °C was maintained using a temperature-controlled water blanket. The tail vein and femoral artery were cannulated using polyethylene catheters for MR contrast agent injection and blood sampling, respectively.

MRI acquisition included T_2-weighted imaging (T_2WI), diffusion-weighted imaging, R_1 mapping and $R_2(^*)$ mapping. The same geometry was applied for all MRI sequences, as follows: field of view = 30 × 30 mm, matrix = 64 × 64, number of slices = 7 and slice thickness = 2 mm. T_2WI was obtained using a fast-spin echo sequence (TR/TE, 5000/22 ms; flip angle, 90°; echo train length, 8). Diffusion-weighted images were acquired using a single-shot echo-planar sequence (TR/TE = 5000/30 ms; number of diffusion directions = 3; and b value = 0, 200 and 800 s/mm^2). The R_1 relaxation rate was measured using a relaxation-enhancement-with-variable-repetition-time sequence, with TR = 251, 300, 500, 700, 1000, 2000, 3000 and 6,000 ms and TE = 7.8 ms. The R_2 relaxation rate was measured using multi-echo spine echo images (TR = 8000 ms, TE range = 10–300 ms, number of TEs = 30, TE interval = 10 ms), and R_2* was measured using multi-echo gradient-echo images (TR = 3000 ms, TE range = 2.5–59.5 ms, number of TEs = 20 and TE interval = 3 ms). The ΔR_2^* and ΔR_2 derived by superparamagnetic iron oxide nanoparticle injection were used to measure the mean total cerebral blood volume (CBV)

and microvascular blood volume (MVV) (vessel radius < 5 μm), respectively[18]. The dose and r_2 of SPION were 5 mg Fe/kg bodyweight and 40 mM^{-1} s^{-1}, respectively. The core diameter of SPOIN ranged from 5 nm to 10 nm, and its mean hydrostatic diameter was 20 ± 5 nm [19, 20].

^{18}F-FDG-PET and PET-MR fusion imaging

^{18}F-FDG PET was obtained to assess the stroke-induced alteration in glucose metabolism, which was obtained using a microPET scanner (Inveon, Siemens Medical Solutions, USA) before MRI acquisition. In total, 300 μCi of ^{18}F-FDG (11.1 MBq of ^{18}F-FDG) in sterile saline (~ 0.3 ml) was injected into the tail vein; thereafter, the rats were maintained in a quiet environment. One hour after the injection, PET images were acquired in three-dimensional mode, with emission scans of 10 min per bed position (matrix size =128 x 128; number of slice = 36; and slice thickness = 0.8 mm).

To obtain a similar geometric alignment to the MRI, the same MRI cradle was used for the PET study. To merge the ^{18}F-FDG PET images with the MR images, an additional series of T_2WIs were obtained, which had similar geometry to PET image (FOV = 30 × 30 mm; matrix size = 128 × 128; number of slice = 36; and slice thickness = 0.8 mm). Thereafter, preliminary PET-MR fusion images was reconstructed to be concordant to diffusion-weighted image, R_1 map and $R_2(^*)$ map. Consequently, a voxel-to-voxel

comparison became available between the MRI and ^{18}F-FDG-PET images.

Data analysis

Imaging data were quantified using the Analysis of Functional NeuroImages (AFNI, National Institute of Health, Bethesda, MD, USA) program and ImageJ (National Institute of Health). Using T_2WI as a reference frame, all MR and PET images were co-registered to achieve the information from the same voxels.

The ADC was quantified according to the following equation:

$$SI(b) = SI(0) \cdot e^{-ADC \cdot B\ value} \quad [1]$$

, where SI is signal intensity at a certain b value and ADC is the apparent diffusion coefficient.

The R_1 relaxation rate was calculated according to the following equation:

$$M(t) = M_0(1 - \alpha \cdot e^{-R_1 \cdot TR}) + C \quad [2]$$

, where M(t) is the signal intensity at a particular TR or TE, M_0 is the steady-state magnetization including spin density and T_1 recovery, α is the efficacy of incomplete saturation in longitudinal magnetization and C is a constant. Then, the hyperoxia-induced ΔR_1 was calculated by $R_{1\_hyperoxia} - R_{1\_normoxia}$.

The R_2(*) was calculated by the following equation:

$$SI(b) = M_0 \cdot e^{-R_2(^*)\cdot t} \quad [3]$$

, where SI is the MR signal intensity, M_0 is the proton density, t is the echo time and $R_2(^*)$ is the transverse relaxation rate, namely, R_2 or R_2^*. Then, the ΔR_2^* (i.e. CBV) and ΔR_2 (i.e. MVV) derived by superparamagnetic iron oxide nanoparticle injection were calculated.

The SUV of the ^{18}F-FDG was calculated by the following equation:

$$\mathrm{SUV} = \frac{tissue\ radioactivity\ conc.}{injected\ activity / body\ weight} = \frac{RI * body\ weight(g)}{injection\ dose(Bq) * e^{(-ln2 * \frac{duration}{half-life})}} \quad [4]$$

, where RI is the tissue radioactivity intensity of the ^{18}F-FDG, duration (60 min) is the time between tracer injection and PET scan initiation and the half-life of radioactive ^{18}F is 109.77 min, respectively.

To analyse the correlation between the MRI and PET parameters, four isometric lines passing the presumed stroke centre were drawn in the stroke area. From these lines, the voxel values of ΔR_1, ADC, R_2, CBV, MVV, and ^{18}F-FDG uptake were extracted. Thereafter, the relationship between the hyperoxia-induced ΔR_1 and the other imaging parameters were analysed with scatterplots.

To assess whether the hyperoxia-induced ΔR_1 can be a criteria to classify the degree of ischemic brain damage, the change pattern of ADC, R_2, CVB, MVV and ^{18}F-

FDG uptake according to the hyperoxia-induced ΔR_1 was analysed by using the sliding window correlation method [21]. With this method, while consecutively sliding the ΔR_1 window (window length = half of total ΔR_1 points; 100 points in this study) from the minimum to the maximum value, the linear fitting at each ΔR_1 window yielded slopes of ADC , R_2, CBV, MVV and ^{18}F-FDG uptake. The calculated slopes indicated the change pattern of stroke-tissue damage according to the hyperoxia-induced ΔR_1.

Statistical analysis

Measurements were compared between the ipsilateral and contralateral hemispheres in the stroke rats and/or between the right and left hemispheres in the normal rats. Within the ipsilateral hemisphere, image parameters were compared among areas with different ischemic burden. The Wilcoxon signed-rank statistics was used for paired comparisons and the Wilcoxon rank-sum test for unpaired comparisons. To evaluate the correlation between the oxygen-induced ΔR_1 and either the ADC , R_2, CBV, MVV and ^{18}F-FDG uptake, the Spearman correlation test was used. A *P*-value of less than 0.05 was considered statistically significant.

Results

The study design and important results are summarized in Figure 1 and representative case is presented in Figure 2.

Stroke characterization by ADC

The stroke area demonstrated high signal intensity on diffusion-weighted images and low apparent diffusion coefficient (ADC). In terms of ischemic severity, each ipsilateral hemisphere of stroke rat was divided into three areas according to the ADC by referring to previous reports (Fig. 2a) [22-25]: (a) severe ischemic area with an ADC less than 80% of that in the anatomically corresponding contralateral hemisphere; (b) intermediate ischemic area with an ADC 80% to 95% of that of the corresponding contralateral ADC; and (c) weak/no ischemic area with an ADC greater than 95% of that of the corresponding contralateral ADC. Accordingly, the strong (mean ± s.d. ADC value, $515 \pm 120 \times 10^{-3}$ $mm^2 \cdot s^{-1}$), intermediate ($619 \pm 116 \times 10^{-3}$ $mm^2 \cdot s^{-1}$) and weak/no ($797 \pm 95 \times 10^{-3}$ $mm^2 \cdot s^{-1}$) ischemic areas showed significantly different ADC values ($P < 0.01$) (Fig. 2a). The ADC value was similar between the contralateral hemisphere of the ischemic brain ($805 \pm 98 \times 10^{-3}$ $mm^2 \cdot s^{-1}$) and normal healthy brain ($809 \pm 87 \times 10^{-3}$ $mm^2 \cdot s^{-1}$) ($P > 0.05$).

PtO_2, PaO_2 and SaO_2

In the PtO_2 measurement using a fibreoptic oximetry unit (Fig. 3a), the hyperoxia-

induced ΔPtO_2 was significantly greater (i.e. greater amount of oxygen accumulation) in the ischemic brain than in the non-ischemic brain (including the contralateral hemisphere of stroke rats and normal healthy brain). Consequently, the area-under-curve of PtO_2 was significantly greater in the ischemic brain (560±95 mmHg) than non-ischemic brain (47±23 mmHg) ($P < 0.001$) (Fig. 3b and 3c). Moreover, a higher normoxic PtO_2 level in the ischemic brain (mean, 48.67 mmHg) than in the non-ischemic brain (mean values, 3.45–5.34 mmHg) ($P < 0.01$) strongly suggested that ischemic injury affected the baseline oxygen level as well as the capacity of oxygen accumulation (Fig 3b).

Importantly, the pattern of the PtO_2 increase during the hyperoxic challenge was apparently different between the ischemic and non-ischemic brain (Fig. 3b). The non-ischemic brain showed controlled oxygen accumulation during hyperoxic respiration as the PtO_2 rapidly increased and reached a plateau 40 to 50 seconds after the initiation of oxygen breathing. In contrast, the ischemic brain presented an unregulated oxygen deposition as its PtO_2 persistently rose during the entire period of hyperoxic respiration. These results indicated uncontrolled plasma-to-tissue oxygen flux due to impaired neurovascular barrier function in the ischemic brain.

The non-ischemic hemispheres demonstrated similar PtO_2 values in both normoxia and hyperoxia ($P > 0.05$). After being switched from hyperoxic to normoxic respiration mode, the PtO_2 decreased in both ischemic and non-ischemic brain.

In the blood gas analysis, hyperoxic respiration increased the PaO_2 by 7.6 times (mean, 479.5 ± 44.7 mmHg) from the normoxic level (63.0 ± 10.2 mmHg) and fully converted deoxyHb to oxyHb (SaO_2 = 100%).

Hyperoxia-induced ΔR_1

The hyperoxic respiration yielded positive ΔR_1 in both ischemic and non-ischemic hemispheres. Specifically, the ΔR_1 during hyperoxic respiration was significantly greater in the ischemic brain (mean ΔR_1, 30 ms^{-1}) than in the non-ischemic brain (mean ΔR_1, 13–16 ms^{-1}) ($P < 0.01$) (Fig. 2b), whereas it was similar between non-ischemic hemispheres ($P > 0.05$).

In the voxel-based analysis of the co-registered ΔR_1 and ADC maps, the ischemic hemisphere showed a trend of inverse correlation between these parameters (Fig. 4a). Accordingly, the hyperoxia-induced ΔR_1 was greatest in the strong ischemic area (52 ± 17 msec-^{1}) and was greater in the intermediate ischemic area (32 ± 18 $msec^{-1}$) than in the weak/no ischemic area (18 ± 21 $msec^{-1}$) ($P< 0.05$).

To minimize the regional variability of the hyperoxia-induced ΔR_1 within cerebral hemisphere, the mean ΔR_1 ratio of the ipsilateral lesion over the anatomically corresponding contralateral area was calculated. It was 5.8 in the strong ischemic area, 3.4 in the intermediate ischemic area and 1.9 in the weak/no ischemic area ($P < 0.01$),

confirming the ischemic severity-dependent oxygen accumulation during the hyperoxic challenge.

R_2 indicating vasogenic edema

Because an increase in the amount of intra-voxel water content decreases the R_2 value, the degree of stroke-induced vasogenic edema can be estimated by the R_2 [26]. The R_2 was increased from strong ischemic area to weak/no ischemic area (R_2: 11.6 ± 1.0 $msec^{-1}$ in the strong ischemic area; 13.7± 1.2 $msec^{-1}$ in the intermediate ischemic area; and 16.2±2.2 $msec^{-1}$ in the weak/no ischemic area) ($P< 0.05$), thereby demonstrating ischemic severity-dependent degree of vasogenic edema (Fig . 2c). Correspondingly, the ipsilateral-to-contralateral R_2 ratio was also associated with ischemic severity (ratio: 0.70 in the strong ischemic area; 0.84 in the intermediate ischemic area; and 0.96 in the weak/no ischemic area) ($P< 0.01$).

In the voxel-based analysis, the distribution of R_2 according to the hyperoxia-induced ΔR_1 showed an exponential decay pattern ($R_2 = 46.96e^{-87.10\Delta R_1} + 10.06, R^2 = 0.4685$) (Fig. 4b), thereby demonstrating a close relationship between impaired permeability barrier and oxygen accumulation in the ischemic brain.

Blood volume parameter

Generalized vasodilation was observed in the ischemic brain as the 25.0 ± 6.3 $msec^{-1}$ in the strong ischemic area, 25.2 ± 7.1 $msec^{-1}$ in the intermediate ischemic area, and 22.9 ± 6.7 $msec^{-1}$ in the weak/no ischemic area (ipsilateral-to-contralateral ratios: 1.40, 1.40 and 1.09 in the strong, intermediate and weak/no ischemic area), respectively (P > 0.05) (Fig. 2d). In contrast, the MVV showed an ischaemia-dependent decrease as it was 1.3 ± 0.8 $msec^{-1}$ in the strong ischemic area, 1.6 ± 0.7 $msec^{-1}$ in the intermediate ischemic area and 1.9 ± 0.7 $msec^{-1}$ in the weak/no ischemic area, respectively (ipsilateral-to-contralateral ratio: 0.68, 0.88, and 0.99 in the strong, intermediate and weak/no ischemic area) (P < 0.01) (Fig. 2e). This decoupled change in CBV and MVV can be interpreted as the collapse and/or constriction of capillary-scale microvessels and the compensatory vasodilation of large vessels in the ischemic brain.

The voxel-wise analysis demonstrated a significant linear correlation between the MVV and R_2 $(R_2 = 2.38\text{MVV} + 8.43, R^2 = 0.597, P \text{ value for F test} < 0.0001)$. Moreover, similarly to the distribution of R_2, the MVV showed an exponential-decay correlation with the hyperoxia-induced ΔR_1 ($\text{MVV} = 9.17e^{-74.94\Delta R_1} + 0.77, R^2 = 0.3398$) (Fig. 4c). The CBV did not show any meaningful correlation with the other image parameters.

The hyperoxic challenge decreased the CBV and MVV, namely, vasoconstriction, by 4% to 13% in bilateral hemispheres in the stroke rats. Because the decreased blood volume in hyperoxic challenge means reduced deoxyHb concentration in each voxel, these findings therefore constitute additional evidence that the increased R_1 during hyperoxia was not produced by deoxyHb.

^{18}F-FDG uptake

In all stroke rats, the ipsilateral hemispheres showed decreased standardization of uptake values (SUV) of the ^{18}F-FDG, i.e. deactivated glucose metabolism, compared with the contralateral hemispheres ($P < 0.05$) (Fig. 2f). In addition, the PET demonstrated a 'diaschisis' phenomenon as the SUV was lower even in the contralateral hemisphere of stroke rat than in the normal healthy brain ($P < 0.05$) (Fig. 2f).

The ^{18}F-FDG uptake showed an ischaemia-dependent decrease pattern as it was 2.2 ± 0.5 in the strong ischemic area, 2.7 ± 0.5 in the intermediate ischemic area and 3.3 ± 0.4 in the weak/no ischemic area, respectively (ipsilateral-to-contralateral ratio: 0.56, 0.68, and 0.84 in the strong, intermediate and weak/no ischemic area) ($P < 0.01$). The ^{18}F-FDG uptake also had a significant exponential-decay correlation with the hyperoxia-induced ΔR_1 ($SUV = 7.29e^{-56.14\Delta R_1} + 1.54,\ R^2 = 0.5749$) (Fig. 4d), thereby strongly

suggesting deactivated oxygen metabolism to be an important cause of excessive oxygen accumulation during hyperoxic challenge in the ischemic brain.

Ischemic damage classification by hyperoxia-induced ΔR_1

As demonstrated in Figure 4e, the slope of ADC, MVV, R_2 and ^{18}F-FDG turned from 'steep' to 'gradual or flat' pattern around ΔR_1 of 50 – 60 msec^{-1}. Corresponding to this change patterns, the mean values of ADC, R_2, MVV, and ^{18}F-FDG were different between voxels with ΔR_1 less than 50 msec^{-1} and those with ΔR_1 equal to or greater than 50 msec^{-1} ($P < 0.01$) (Box-and-Whisker graphs in Fig 4 a-d). There was no significant correlation between the slope of CBV and the hyperoxia-induced ΔR_1.

Discussion

The principal idea of this study was that oxygen accumulation in hyperoxic challenge can be measured by the hyperoxia-induced ΔR_1. As evidential results to this concept, the hyperoxic respiration significantly increased PtO_2 and PaO_2, and the ischemic hemisphere demonstrated greater hyperoxia-induced ΔPtO_2 and ΔR_1 than the non-ischemic brain. Theoretically, the influence of blood deoxyHb on R_1 could be excluded as tissue water cannot be sufficiently proximal (i.e. 3Å) to the coordination sites of heme iron for spin–lattice interactions to form [13]. Therefore, increase of R_1 during hyperoxic challenge

was generated directly by the paramagnetism of oxygen molecules, thereby indicating the amount of hyperoxia-induced tissue oxygen accumulation. Accordingly, the higher ΔR_1 in the ischemic brain than in the non-ischemic brain indicates stroke-related excessive oxygen accumulation during hyperoxic respiration. Moreover, an inverse correlation between ΔR_1 and ADC strongly suggests that ischemic injury modified or damaged the biological mechanism to determine the tissue oxygen level. Meanwhile, the hyperoxia-induced ΔR_1 and ΔPtO_2 in the non-ischemic brain demonstrated a homeostatic capacity to maintain a tolerable PtO_2 range.

Oxygen supply and consumption are two major determinants of tissue oxygen concentration. An altered or disrupted balance between these two components is believed to be a cause of excessive oxygen deposition during hyperoxic challenge in the ischemic brain. Therefore, both increased neurovascular supply and deactivated glycolytic oxygen metabolism should be considered to be the main factors underlying the elevation of ΔR_1 in the ischemic brain.

The neurovascular oxygen supply can be compartmentalized into vascular oxygen delivery and plasma-to-tissue oxygen flux. In terms of vascular delivery, this study demonstrated reduced MVV, which means insufficiency in the trans-capillary oxygen exchange area. In addition, the hyperoxic respiration induced generalized vasoconstriction (decreased CBV and MVV). Accordingly, such decreased vascular oxygen delivery cannot

explain the increased hyperoxia-induced ΔR_1 in the ischemic brain.

Instead of vascular delivery, an amplified plasma-to-tissue oxygen flux is highly suggested to exaggerate the oxygen supply in the ischemic brain. Specifically, up-regulated oxygen extraction fraction and uncompensated oxygen flux can be regarded as factors to boost oxygen tissue entry. The former is a well-known compensatory mechanism to provide a sufficient amount of oxygen to ischemic neurons, whereas the latter means the disruption of the protective neurovascular barrier. Although both processes may overlap in the course of stroke progression in our 24-hour middle cerebral artery occlusion rats, we suggest that the impaired neurovascular barrier function more significantly impacted the ΔR_1 and ΔPtO_2 than the controlled increase of oxygen extraction fraction. This explanation is supported by the following results of our fibreoptic oximetry experiments and the voxel-based comparison of MRI parameters: (a) the ischemic hemisphere showed a persistent increase in PtO_2 during oxygen inhalation, whereas the PtO_2 in the non-ischemic brain rapidly plateaued soon after hyperoxic challenge initiation; and (b) the hyperoxia-induced ΔR_1 significantly correlated with the degree of vasogenic edema (defined by R_2). These results strongly agree with previous study findings, in which the damaged neurovascular barrier function manifested extravasation of Evan Blue dye and IgG in a 24-h MCAO stroke model [27, 28].

Along with the above-mentioned relationship between excessive oxygen

accumulation and vasogenic edema in ischemic hemisphere, an inverse correlation between the hyperoxia-induced ΔR_1 and MVV is suggested as another manifestation of stroke-induced neurovascular damage. In support of this explanation, the 'no flow' phenomenon can be taken into account, in which damaged microvessels concomitantly exhibit both plasma transudation and luminal obstruction in stroke rat brain [29]. As the decreased R_2 and decreased MVV are concordant to such findings of 'no flow' phenomenon, we suggest that stroke-associated neurovascular injury amplified plasma-to-tissue oxygen transfer during oxygen challenge, which eventually increased the hyperoxia-induced ΔR_1 and ΔPtO_2.

With regard to deactivated metabolic oxygen consumption in stroke, this study showed a significant decrease in ^{18}F-FDG uptake in the ischemic brain, as noted in previous studies [30, 31]. The SUV demonstrated a strong inverse correlation with the hyperoxia-induced ΔR_1 in the ischemic brain. Therefore, along with the increased tissue oxygen transfer, decreased metabolic oxygen consumption is a major mechanism underlying the increased hyperoxia-induced ΔR_1 in the ischemic brain.

The PET experiments also demonstrated a lower SUV in the contralateral hemisphere of stroke rats (3.88) compared with normal healthy brain (4.72–4.74). Being named as diaschisis, this finding indicates abnormalities in metabolism or neuronal activity in anatomically intact brain regions distant from the lesion [32]. Interestingly, such a

metabolic decrease was not coupled with the hyperoxia-induced ΔR_1 (similar ΔR_1 between the contralateral hemisphere and normal healthy brain). As such mismatched oxygen concentration and glucose metabolism in diaschisis was also found in previous work [33], these results imply that the contralateral hemisphere maintains an adequate PtO_2 range independently of neuronal metabolism. Although there has been no convincing explanation for this phenomenon, we presume that the autoregulated neurovascular oxygen supply may contribute to the homeostasis of the tissue oxygen level over the altered glucose metabolism.

Importantly, the imaging parameter of ischemic cerebral damage (i.e. ADC, R_2, MVV and ^{18}F-FDG) could be classified by the hyperoxia-induced ΔR_1 as their slopes and distribution were dichotomized around the ΔR_1 of 50 – 60 $msec^{-1}$. In voxels with ΔR_1 less than 50 $msec^{-1}$, these stroke-related parameters rapidly decreased according to the ΔR_1, whereas their change was plateaued when ΔR_1 was greater than 60 $msec^{-1}$. Consequently, the ischemic damage could be classified as 'exacerbating' and 'devastate' stages by the ΔR_1. The rapid change of stroke parameters according to the ΔR_1 suggests that the tissue oxygenation status is significantly sensitive to ischemia-driven biologic alterations. In other words, cerebral tissue under active progression of ischemic damage may also have a restoration potential when adequately treatment is applied. In contrast, plateaued change of stroke-related parameters in tissue with ΔR_1 greater than 60 $msec^{-1}$ may indicate an

irreversible ischemic damage. Therefore, these distributional profiles may demonstrate a potential of hyperoxia-induced ΔR_1 as an indicator of ischemic penumbra.

This study attempted to evaluate the feasibility and capability of hyperoxia-induced ΔR_1 to assess cerebral damage in stroke. To minimize the fluctuations in disease severity and the influence of inter- and intra-subject variability, a steady state of ischemic damage was required rather than a dynamic phonological manifestation during the stroke progression. Therefore, our experiments were performed 24 h after the onset of transient ischaemia because this time window was suggested to reduce the variation in micro-environmental changes. Thus, our study results do not reflect the biological phenomenon in hyperacute or acute stroke. Nevertheless, based on the close relationship with ADC, MVV, R_2 and ^{18}F-FDG uptake, the hyperoxia-induced ΔR_1 may demonstrate a capability to indicate the turning point from reversible to irreversible tissue injury.

As an imaging biomarker to assess the ischemic brain damage, hyperoxia-induced ΔR_1 has a number of advantages. The relative simplicity in the image acquisition and parameter calculation is an important strength over imaging methods requiring complex algorithms, injection of extrinsic contrast material and radiation hazard control. Regarding the time window of application, the hyperoxia-induced ΔR_1 can be applied at various stages of cerebral ischaemia, although the ADC is relevant only for evaluating cellular edema in acute stroke. Based on these benefits, the hyperoxia-induced ΔR_1 can be

adequately used to evaluate the damage and restoration of neurovascular and metabolic function in the management of stroke patients. To improve its applicability in clinical practice, further investigation is needed to validate the accuracy of rapid R_1 mapping methods, for example, a single-shot inversion-recovery sequence with radial under-sampling at a temporal resolution of 82.25 ms[34].

In summary, our study demonstrated a significant increase of hyperoxia-induced ΔR_1 in ischemic hemisphere of stroke rat in a fashion depending the ischemic severity. We verified excessive oxygen accumulation during hyperoxic challenge to be a principal source of the ΔR_1 in the stroke brain. As the main causes of the ΔR_1 increase, our study validated uncontrolled plasma-to-tissue oxygen flux due to neurovascular disruption and reduced oxygen consumption due to deactivated glucose metabolism. Moreover, from the ΔR1-depending dichotomized distribution of MRI and PET parameters of cellular/vasogenic edema, capillary volume and glucose metabolism, we suggest that hyperoxia-induced ΔR_1 can classify the status of ischemic brain as "exacerbating stage' and 'devastated stage'. Given its technical simplicity and applicability, hyperoxia-induced ΔR_1 can be a promising MRI biomarker to assess stroke-induced cerebral damage.

Figure1. Summarized study design and results. According to the paramagnetism of oxygen molecule to accelerate the longitudinal relaxation, increasing tissue oxygen concentration by hyperoxic respiration elevates the R_1 value. In stroke brain, neurovascular degradation amplifies the plasma-to-tissue oxygen flux, and neuronal damage deactivates the metabolic oxygen consumption. These biological alterations eventually results in excessive oxygen accumulation during hyperoxic respiration in ischemic brain, as validated in our experiment. Based on such physical and biological background, we measured the hyperoxia-induced ΔR_1 as a quantitative indicator of tissue oxygen accumulation during hyperoxic challenge. Our study showed ischemic severity-dependent increase of the hyperoxia-induced ΔR_1. Moreover, the distribution and change of stroke-related imaging parameters (cellularvasogenic edema, microvascular volume and glucose metabolism activity) were dichotomized by the ΔR1, thereby suggesting that the hyperoxia-induced ΔR1may classify the ischemic damage as 'exacerbating' and 'devastated' stages. Thus, hyperoxia-induced ΔR_1 can be a promising MRI biomarker of impaired neurovascular integrity and neuronal metabolism in stroke.

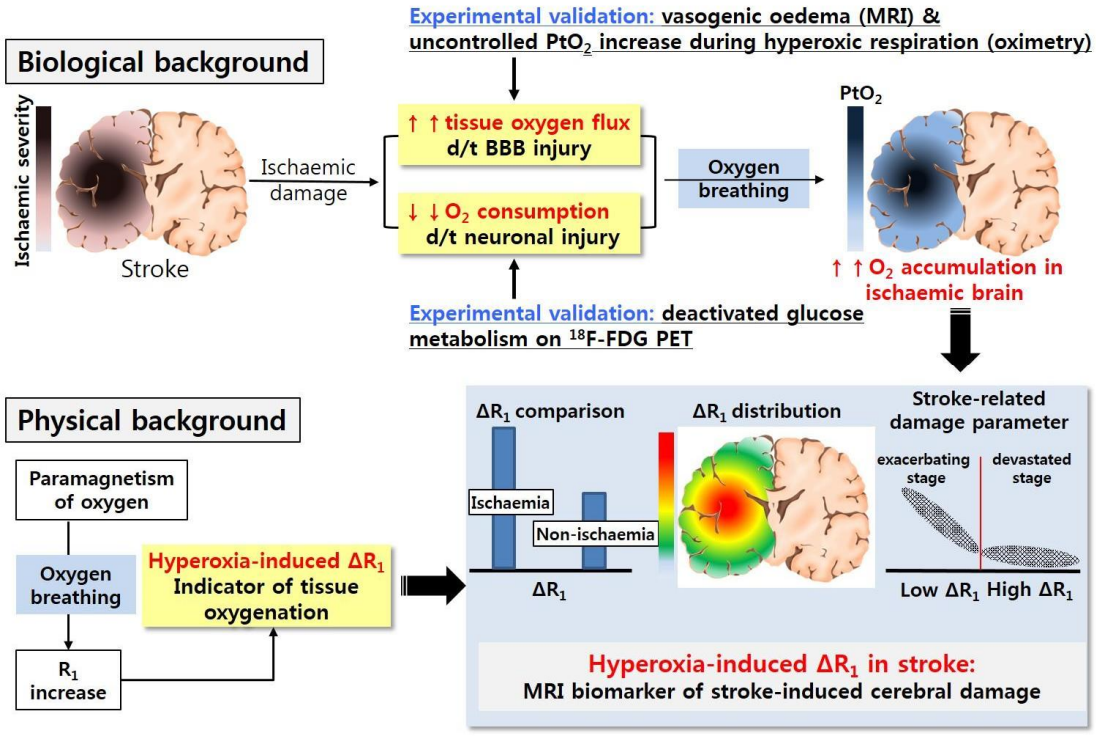

Figure 2. Stroke-induced alteration in variable imaging parameters.

(a) ADC. The ADC is decreased in the ischemic hemisphere (grey map). In terms of ischemic severity, the ischemic hemisphere can be divided into three areas according to the ADC, including severe (red), intermediate (orange) and weak/no ischemic (green) areas (colour map). Accordingly, these three areas show significantly different ADC values (bar graph).

(b) Hyperoxia-induced ΔR_1. The ΔR_1 is increased in the ischemic hemisphere (colour map) with a fashion depending on the ischemic severity (bar graph).

(c) R_2 indicating vasogenic edema. The R_2 is decreased in the ischemic hemisphere (colour map) with a fashion depending on the ischemic severity (bar graph).

(d) CBV. The CBV is increased in the ischemic hemisphere (colour map), thereby presenting compensatory vasodilation (no significant difference according to the ischemic severity on bar graph).

(e) MVV. The MVV is decreased in the ischemic hemisphere (colour map) with a fashion depending on the ischemic severity (bar graph).

(f) ^{18}F-FDG uptake on PET. The SUV is decreased in the ischemic hemisphere (colour map) with a fashion depending on the ischemic severity (bar graph). The contralateral hemisphere of stroke rat shows a lower SUV than normal healthy brain, thereby presenting diaschisis.

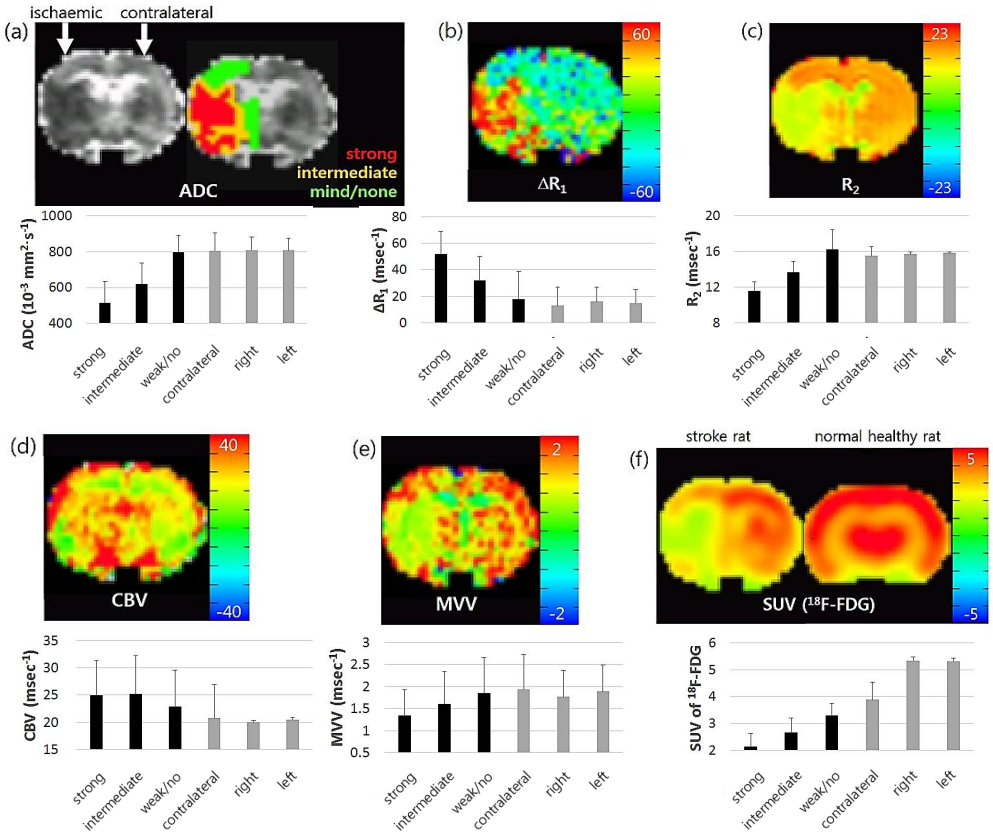
(a)
ischaemic
contralateral
ADC
strong
intermediate
mind/none
(b)
60
-60
ΔR1
(c)
23
-23
R2
ADC (10-3 mm2-s-1)
1000
800
600
400
ΔR1 (msec-1)
80
60
40
20
0
R2 (msec-1)
20
16
12
8
strong
intermediate
weak/no
contralateral
right
left
(d)
40
-40
CBV
(e)
2
-2
MVV
(f)
stroke rat
normal healthy rat
5
-5
SUV (18F-FDG)
CBV (msec-1)
35
30
25
20
15
MVV (msec-1)
3
2.5
2
1.5
1
0.5
SUV of 18F-FDG
6
5
4
3
2

Figure 3. PtO_2 change during hyperoxic challenge in fiberoptic oximetry experiment.

(a) The oximetry probes were bilaterally inserted in each of stroke and normal rats.

(b) Time-dependent PtO_2 change (mean value) according to gas paradigm in the ischemic brain (blue line) and non-ischemic brain (red line) (contralateral hemisphere of stroke rats and normal healthy brain). The pattern of PtO_2 increase during the hyperoxic challenge was apparently different between the ischemic (continuous increase) and non-ischemic (rapidly plateaued) brain. Moreover, the normoxic PtO_2 was greater in the ischemic brain than non-ischemic brain, thereby indicating altered baseline oxygenation in stroke.

(c) Comparison of area-under-PtO_2 curve. The hyperoxia-induced ΔPtO_2 was significantly greater in the ischemic brain than in the non-ischemic brain, while being similar between contralateral hemisphere of stroke rat and normal healthy brain.

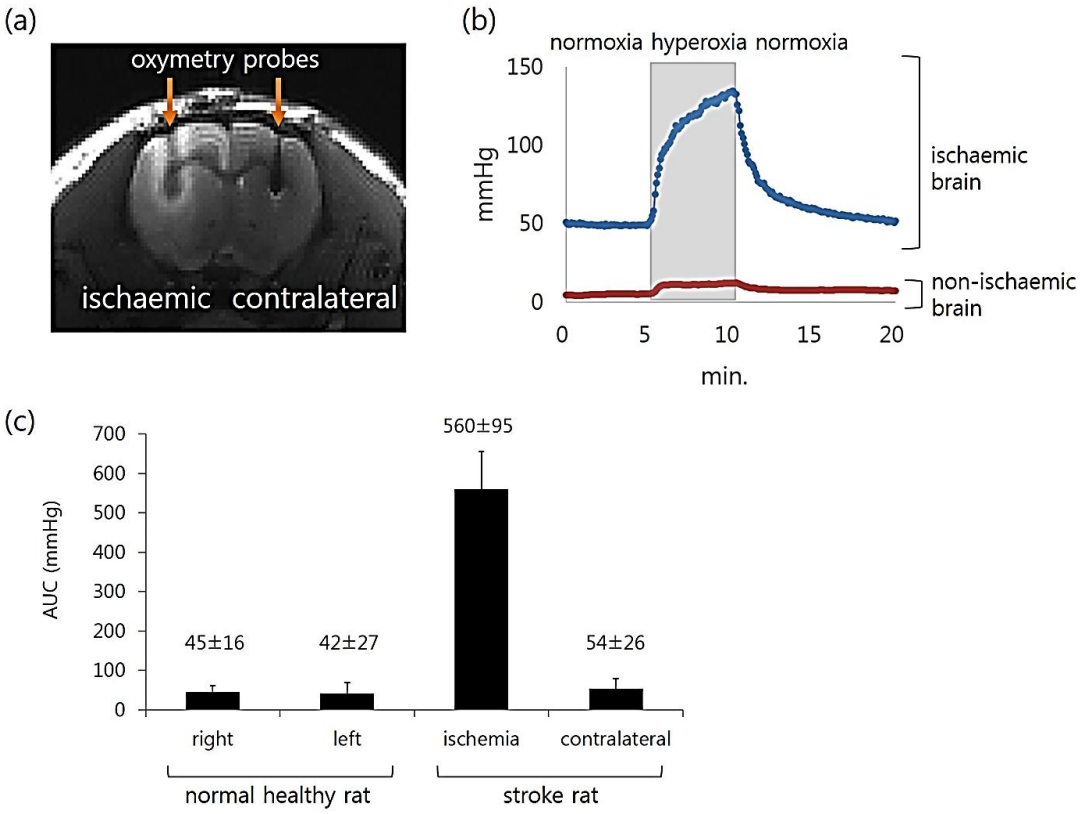

Figure 4. Voxel-wise correlation of imaging parameters in the ischemic hemisphere. In scatterplots, the linearly fitted lines in each ΔR_1 window are shown as red lines. Therefore, the distribution of the red lines presents a change pattern of stroke-related parameters according to the hyperoxia-induced ΔR_1.

(a-d) Scatterplots and comparison graphs of ADC (a), R_2 (b), MVV (c) and SUV of ^{18}F-FDG (d). In the scatterplots, stroke-related parameters show bi-exponential decay pattern according to the ΔR_1. Therefore, their mean values were significantly different between voxels with ΔR_1 less than 50 $msec^{-1}$ and those with ΔR_1 equal to or greater than 50 $msec^{-1}$ (Box-and-Whisker graphs).

(e) Distribution of slopes of stroke-related parameters according to the hyperoxia-induced ΔR_1. The slopes of ADC, R_2, MVV and ^{18}F-FDG in each sliding window turn from 'steep' to 'gradual or flat' pattern around ΔR_1 of 50 – 60 $msec^{-1}$ (dots, raw data of slopes; lines, fitted line of slopes). For ease of comparison, the slope was calculated after converting each data to standardized values by using the following equation:

$$z = \frac{(X - \mu)}{\sigma}$$

, where X is the value, μ is the mean, and σ is the standard deviation.

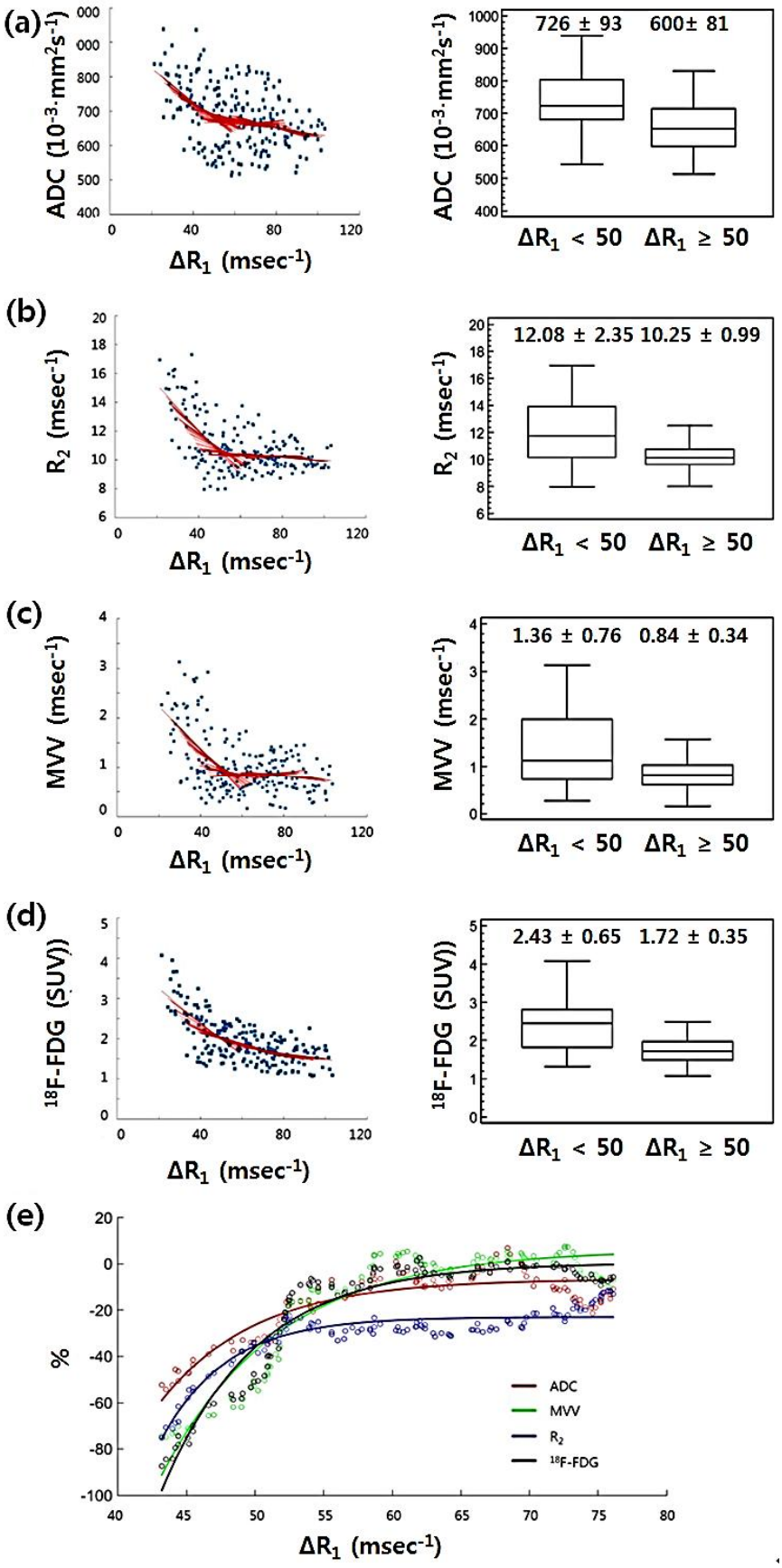
(a)
ADC (10-3·mm2s-1)
ΔR1 (msec-1)
726 ± 93
600± 81
ΔR1 < 50
ΔR1 ≥ 50
(b)
R2 (msec-1)
12.08 ± 2.35
10.25 ± 0.99
(c)
MVV (msec-1)
1.36 ± 0.76
0.84 ± 0.34
(d)
18F-FDG (SUV))
2.43 ± 0.65
1.72 ± 0.35
(e)
%
ADC
MVV
R2
18F-FDG

References

1. Bratton SL, Chestnut RM, Ghajar J, McConnell Hammond FF, Harris OA, Hartl R et al. Guidelines for the management of severe traumatic brain injury. X. Brain oxygen monitoring and thresholds. Journal of neurotrauma 2007;24 Suppl 1:S65-70
2. Stiefel MF, Spiotta A, Gracias VH, Garuffe AM, Guillamondegui O, Maloney-Wilensky E et al. Reduced mortality rate in patients with severe traumatic brain injury treated with brain tissue oxygen monitoring. Journal of neurosurgery 2005;103:805-11
3. van den Brink WA, van Santbrink H, Steyerberg EW, Avezaat CJ, Suazo JA, Hogesteeger C et al. Brain oxygen tension in severe head injury. Neurosurgery 2000;46:868-76; discussion 76-8
4. Schwarzbauer C, Deichmann R. Vascular component analysis of hyperoxic and hypercapnic bold contrast. Neuroimage 2012;59:2401-12
5. Ogawa S, Lee T, Kay A, Tank D. Brain magnetic resonance imaging with contrast dependent on blood oxygenation. Proceedings of the National Academy of Sciences 1990;87:9868-72
6. Belfatto A, White DA, Zhongwei Z, Zhang Z, Cerveri P, Baroni G et al. Mathematical modeling of tumor response to radiation: Radio-sensitivity correlation with bold, told, deltar1 and deltar2* investigated in large dunning r3327-at1 rat prostate tumors. Conference proceedings : ... Annual International Conference of the IEEE Engineering in Medicine and Biology Society. IEEE Engineering in Medicine and Biology Society. Annual Conference 2015;2015:3266-9
7. Ikoma Y, Watabe H, Shidahara M, Naganawa M, Kimura Y. Pet kinetic analysis: Error consideration of quantitative analysis in dynamic studies. Ann Nucl Med 2008;22:1-11
8. Li F, Joergensen JT, Hansen AE, Kjaer A. Kinetic modeling in pet imaging of hypoxia. Am J Nucl Med Mol Imaging 2014;4:490-506

9. Song Y, Chun S-I, Kim H, Lim DW, Kim YR, Kim JK et al. The role of oxygen molecule dissolved in rat blood based on bold mri. In. Melbourne, Austrailia, 2012; 3071.
10. Pilkinton DT, Gaddam SR, Reddy R. Characterization of paramagnetic effects of molecular oxygen on blood oxygenation level-dependent-modulated hyperoxic contrast studies of the human brain. Magn Reson Med 2011;66:794-801
11. Jordan BF, Magat J, Colliez F, Ozel E, Fruytier AC, Marchand V et al. Mapping of oxygen by imaging lipids relaxation enhancement: A potential sensitive endogenous mri contrast to map variations in tissue oxygenation. Magnetic resonance in medicine : official journal of the Society of Magnetic Resonance in Medicine / Society of Magnetic Resonance in Medicine 2012
12. Colliez F, Neveu MA, Magat J, Cao Pham TT, Gallez B, Jordan BF. Qualification of a noninvasive magnetic resonance imaging biomarker to assess tumor oxygenation. Clinical cancer research : an official journal of the American Association for Cancer Research 2014
13. Song Y, Cho G, Chun SI, Baek JH, Cho H, Kim YR et al. Oxygen-induced frequency shifts in hyperoxia: A significant component of bold signal. NMR Biomed 2014;27:835-42
14. Dewhirst MW, Birer SR. Oxygen-enhanced mri is a major advance in tumor hypoxia imaging. Cancer research 2016;76:769-72
15. O'Connor JP, Boult JK, Jamin Y, Babur M, Finegan KG, Williams KJ et al. Oxygen-enhanced mri accurately identifies, quantifies, and maps tumor hypoxia in preclinical cancer models. Cancer research 2016;76:787-95
16. Colliez F, Safronova MM, Magat J, Joudiou N, Peeters AP, Jordan BF et al. Oxygen mapping within healthy and acutely infarcted brain tissue in humans using the nmr relaxation of lipids: A proof-of-concept translational study. PloS one 2015;10:e0135248
17. Longa EZ, Weinstein PR, Carlson S, Cummins R. Reversible middle cerebral artery occlusion without craniectomy in rats. Stroke 1989;20:84-91

18. Boxerman JL, Hamberg LM, Rosen BR, Weisskoff RM. Mr contrast due to intravascular magnetic susceptibility perturbations. Magnetic resonance in medicine : official journal of the Society of Magnetic Resonance in Medicine / Society of Magnetic Resonance in Medicine 1995;34:555-66
19. Kwon HJ, Shim WH, Cho G, Cho HJ, Jung HS, Lee CK et al. Simultaneous evaluation of vascular morphology, blood volume and transvascular permeability using spion-based, dual-contrast mri: Imaging optimization and feasibility test. NMR in biomedicine 2015;28:624-32
20. Kim JH, Suh JY, Woo DC, Sung YS, Son WC, Choi YS et al. Difference in the intratumoral distributions of extracellular-fluid and intravascular mr contrast agents in glioblastoma growth. NMR in biomedicine 2016;29:1688-99
21. Shakil S, Lee CH, Keilholz SD. Evaluation of sliding window correlation performance for characterizing dynamic functional connectivity and brain states. Neuroimage 2016;133:111-28
22. Desmond PM, Lovell AC, Rawlinson AA, Parsons MW, Barber PA, Yang Q et al. The value of apparent diffusion coefficient maps in early cerebral ischemia. AJNR Am J Neuroradiol 2001;22:1260-7
23. Na DG, Thijs VN, Albers GW, Moseley ME, Marks MP. Diffusion-weighted mr imaging in acute ischemia: Value of apparent diffusion coefficient and signal intensity thresholds in predicting tissue at risk and final infarct size. AJNR Am J Neuroradiol 2004;25:1331-6
24. Sakoh M, Ostergaard L, Gjedde A, Rohl L, Vestergaard-Poulsen P, Smith DF et al. Prediction of tissue survival after middle cerebral artery occlusion based on changes in the apparent diffusion of water. Journal of neurosurgery 2001;95:450-8
25. Oppenheim C, Grandin C, Samson Y, Smith A, Duprez T, Marsault C et al. Is there an apparent diffusion coefficient threshold in predicting tissue viability in hyperacute stroke? Stroke; a journal of cerebral circulation 2001;32:2486-91
26. An H, Ford AL, Vo KD, Liu Q, Chen Y, Lee JM et al. Imaging oxygen metabolism in acute stroke using mri. Current radiology reports 2014;2:39

27. Liu F, Yuan R, Benashski SE, McCullough LD. Changes in experimental stroke outcome across the life span. J Cereb Blood Flow Metab 2009;29:792-802
28. Haley MJ, Lawrence CB. The blood-brain barrier after stroke: Structural studies and the role of transcytotic vesicles. J Cereb Blood Flow Metab 2017;37:456-70
29. del Zoppo GJ, Mabuchi T. Cerebral microvessel responses to focal ischemia. J Cereb Blood Flow Metab 2003;23:879-94
30. Sobrado M, Delgado M, Fernandez-Valle E, Garcia-Garcia L, Torres M, Sanchez-Prieto J et al. Longitudinal studies of ischemic penumbra by using 18f-fdg pet and mri techniques in permanent and transient focal cerebral ischemia in rats. Neuroimage 2011;57:45-54
31. Bunevicius A, Yuan H, Lin W. The potential roles of 18f-fdg-pet in management of acute stroke patients. BioMed research international 2013;2013:634598
32. Carrera E, Tononi G. Diaschisis: Past, present, future. Brain : a journal of neurology 2014;137:2408-22
33. Yamauchi H, Fukuyama H, Nagahama Y, Nishizawa S, Konishi J. Uncoupling of oxygen and glucose metabolism in persistent crossed cerebellar diaschisis. Stroke; a journal of cerebral circulation 1999;30:1424-8
34. Pastor G, Jimenez-Gonzalez M, Plaza-Garcia S, Beraza M, Reese T. Fast t1 and t2 mapping methods: The zoomed u-flare sequence compared with epi and snapshot-flash for abdominal imaging at 11.7 tesla. Magma (New York, N.Y.) 2017;30:299-307

국문요약

조직 산소포화의 비-침습영상은 뇌졸중으로 인한 대뇌 손상의 중요한 정보를 제공한다. 여기에 우리는 과 산소 호흡 시 산소로 인한 R1 변화를 정량화 하는 MRI 매개변수인 과 산소-유도 ΔR1 을 소개한다. 허혈성 심각도(겉보기 확산 계수로 정의됨)는 뇌졸중으로 인한 과도한 산소 축적을 나타내는데, 일시적 뇌졸중 쥐 모델에서 허혈성 뇌는 허혈성 심각도와 같이 과 산소-유도 ΔR1 의 유의한 증가를 보여주었다. ΔR1 이 증가하는 원인 중 하나는 신경혈관의 파열에 의하여 혈장-조직 간 산소 이동이 조절되지 않았기 때문이다. 신경혈관의 파열은 ΔR1 과 혈관성 부종(R2)간의 유의한 상관 관계로 알 수 있고, 허혈성 뇌(비-평형 증가)와 비-허혈성 뇌(빠른 평형 도달) 간의 과 산소로 인해 나타나는 ΔPtO_2 패턴 차이에 의해 나타내어 진다. 또한, 감소된 산소 소모가 ΔR1 과 포도당 대사 활동(^{18}F-FDG 섭취) 사이의 유의한 역 상관관계에 따라 ΔR1 을 증가시키는 것으로 알려져 있다. 허혈성 손상의 영상 매개변수들인 겉보기 확산 계수(ADC), 혈관성 부종(R2), 모세혈관 체적(초전도 산화철 제제에 의한 ΔR2) 그리고 포도당 대사(^{18}F-FDG 섭취)는 ΔR1 에 따른 이분화 된 분포를 보였다. 그러므로, 과 산소-유도 ΔR1 은 “악화중인 상태”와 “괴사된 상태”같이 허혈성 뇌의 상태를 분류할 수 있다. 결론적으로, 과 산소-유도 ΔR1 은 뇌졸중으로 인한 대뇌 손상을 평가하기 위한 유의미한 MRI 바이오마커가 될 수 있다.

중심단어: 조직 산소농도, R1, 비-침습 영상, 자기공명영상 바이오마커, 뇌졸중, 과산

소-유도 ΔR1